

The $z \sim 1.03$ Merging Cluster SPT-CL J0356–5337: New Strong Lensing Analysis with HST and MUSE

GRACE SMITH ¹, GUILLAUME MAHLER ^{2,3,4}, KATE NAPIER ¹, KEREN SHARON ¹, MATTHEW BAYLISS ⁵,
BRADFORD BENSON ^{6,7}, LINDSEY BLEEM ^{8,9}, BENJAMIN FLOYD ^{10,11}, VITTORIO GHIRARDINI ¹²,
MICHAEL D. GLADDERS ^{7,13}, GOURAV KHULLAR ¹⁴ AND TIM SCHRABBACK ¹⁵

¹*Department of Astronomy, University of Michigan, 1085 S. University Ave, Ann Arbor, MI 48109, USA*

²*STAR Institute, Quartier Agora - Allée du six Août, 19c B-4000 Liège, Belgium*

³*Centre for Extragalactic Astronomy, Durham University, South Road, Durham DH1 3LE, UK*

⁴*Institute for Computational Cosmology, Durham University, South Road, Durham DH1 3LE, UK*

⁵*Department of Physics, University of Cincinnati, Cincinnati, OH 45221, USA*

⁶*Fermi National Accelerator Laboratory, MS209, P.O. Box 500, Batavia, IL 60510, USA*

⁷*Department of Astronomy and Astrophysics, University of Chicago, 5640 South Ellis Avenue, Chicago, IL 60637, USA*

⁸*High-Energy Physics Division, Argonne National Laboratory, 9700 South Cass Avenue., Lemont, IL, 60439, USA*

⁹*Kavli Institute for Cosmological Physics, University of Chicago, 5640 South Ellis Avenue, Chicago, IL, 60637, USA*

¹⁰*Faculty of Physics and Astronomy, University of Missouri-Kansas City, 5110 Rockhill Road, Kansas City, MO 64110, USA*

¹¹*Institute of Cosmology and Gravitation, University of Portsmouth, Dennis Sciama Building, Portsmouth PO1 3FX, UK*

¹²*Max-Planck-Institut für Extraterrestrische Physik, Gießenbachstraße, D-85748 Garching, Germany*

¹³*Kavli Institute for Cosmological Physics, University of Chicago, Chicago, IL 60637, USA*

¹⁴*Department of Physics and Astronomy, and PITT PACC, University of Pittsburgh, Pittsburgh, PA 15260, USA*

¹⁵*Universitat Innsbruck, Institut für Astro- und Teilchenphysik, Technikerstr. 25/8, 6020 Innsbruck, Austria*

ABSTRACT

We present a strong lensing analysis and reconstruct the mass distribution of SPT-CL J0356–5337, a galaxy cluster at redshift $z = 1.034$. Our model supersedes previous models by making use of new multi-band HST data and MUSE spectroscopy. We identify two additional lensed galaxies to inform a more well-constrained model using 12 sets of multiple images in 5 separate lensed sources. The three previously-known sources were spectroscopically confirmed by Mahler et al. (2020) at redshifts of $z = 2.363$, $z = 2.364$, and $z = 3.048$. We measured the spectroscopic redshifts of two of the newly-discovered arcs using MUSE data, at $z = 3.0205$ and $z = 5.3288$. We increase the number of cluster member galaxies by a factor of three compared to previous work. We also report the detection of extended Ly α emission from several background galaxies. We measure the total projected mass density of the two major sub-cluster components, one dominated by the BCG, and the other by a compact group of luminous red galaxies. We find $M_{BCG}(< 80\text{kpc}) = 3.93^{+0.21}_{-0.14} \times 10^{13} M_{\odot}$ and $M_{LRG}(< 80\text{kpc}) = 2.92^{+0.16}_{-0.23} \times 10^{13} M_{\odot}$, yielding a mass ratio of $1.35^{+0.16}_{-0.08}$. The strong lensing constraints offer a robust estimate of the projected mass density regardless of modelling assumptions; allowing more substructure in this line of sight does not change the results or conclusions. Our results corroborate the conclusion that SPT-CL J0356–5337 is dominated by two mass components, and is likely undergoing a major merger on the plane of the sky.

Keywords: Galaxy clusters (584); Gravitational lensing (670); Strong gravitational lensing (1643); Dark matter distribution (356)

1. INTRODUCTION

Galaxy clusters, especially those at high redshift, probe large-scale structure formation. Clusters grow by undergoing mergers with other mass components. Whereas minor mergers, involving galaxy- to group-scale halos falling into the cluster-scale halo, are rather

common, major mergers—where the merging component is at least one third of the mass of the cluster—are much rarer (Fakhouri & Ma 2008). Mergers of clusters represent short events in the long history of the clusters, which offer insight into the buildup of large scale structure in the Universe, and into the growth and redistribu-

bution of dark matter and baryons in the densest nodes of the cosmic web. Studying this phase, and separating the masses of the two (or more) merging components, requires a high resolution mass probe, capable of measuring of the mass distribution within radii smaller than 100-500 kpc of the cluster core. The best probe at such scales is strong gravitational lensing, which can map the projected mass density with high resolution.

There are only a few known major mergers that exhibit strong lensing evidence, which can be used to map in detail the dark matter at the core of the merger. Some well-studied examples include the “Bullet Cluster” (1E 0657–558, Clowe et al. 2006; Bradač et al. 2006) and “El Gordo” (ACT–CL J0102-4915, Menanteau et al. 2012; Caminha et al. 2023). While rare, the multi-wavelength studies of such lines of sight advanced our understanding of some of the fundamental properties of the Universe such as providing solid evidence for dark matter (e.g., Clowe et al. 2006) and constraining the dark matter self-interaction cross-section (e.g., Harvey et al. 2015; Markevitch et al. 2004; Wittman et al. 2018; Randall et al. 2008; Bradač et al. 2008).

The subject of this paper is SPT-CLJ 0356–5337 (hereafter SPT-0356), a galaxy cluster at redshift $z = 1.034$ acting as a strong gravitational lens. The cluster was discovered by the South Pole Telescope (SPT) based on its Sunyaev-Zel’dovich (SZ) effect signature (Bleem et al. 2015, 2020). It is reported to have a total mass of $M_{200c} = 5.12_{-1.32}^{+1.00} \times 10^{14} M_{\odot} h_{70}^{-1}$ and $M_{500c} = 3.59_{-0.66}^{+0.59} \times 10^{14} M_{\odot} h_{70}^{-1}$ (Bocquet et al. 2019). Optical imaging and spectroscopic followup of SPT-0356 (Mahler et al. 2020) revealed that it is composed of two main mass components at the same redshift, separated by ~ 170 kpc: the eastern component is associated with the brightest cluster galaxy (BCG), and the western component is associated with a group of luminous red galaxies (LRGs). The two-component mass distribution, paired with the fact that these two components have nearly equal radial velocities (within 300 km s^{-1}), implies that SPT-0356 is undergoing a merger on the plane of the sky. Analysis of the mass distribution would determine whether the system could be classified as a major merger.

In the first lensing analysis of SPT-0356, Mahler et al. (2020) reported that the mass distribution in the lens plane is consistent with two major cluster-scale halos, with a mass ratio between 1:1.25 and 1:1.58. Their lens model relied on ground-based imaging and spectroscopy, and shallow single-band Hubble Space Telescope (HST) imaging data, and was underconstrained, since all the lensing constraints that were identified were between the two merging sub-clusters (Mahler et al. 2020). Multi-

band, high-resolution imaging is necessary for identification of a robust set of lensing constraints, using color and resolved morphology to identify multiple images of the same source.

In this paper, we report new multi-band HST imaging of SPT-0356, obtained to determine whether the system is undergoing a major merger. We also report data and results from the Multi-Unit Spectroscopic Explorer (MUSE), used to measure the redshifts of newly identified lensing constraints, cluster member galaxies and other sources in the field of view. We present results from an updated lens model based on the new constraints.

This paper is organized as follows. We describe the HST and MUSE observations, data reduction, and spectra extraction in Section 2. We describe the identification and assessment of background lensed galaxies and their spectroscopic confirmation in Section 3. We outline the process used to create our strong gravitational lens model in Section 4. We present the lens model results, including a measurement of the masses of the two sub-cluster components in Section 5. We discuss our results in Section 6. Finally, we summarize our findings in Section 7.

This work assumes a flat Λ CDM cosmology with $\Omega_{\Lambda} = 0.7$, $\Omega_m = 0.3$, and $H_0 = 70 \text{ km s}^{-1} \text{ Mpc}^{-1}$. At the redshift of SPT-0356, $z = 1.034$, $1''0 = 8.063 \text{ kpc}$ in this cosmology. Magnitudes are reported in the AB system.

2. DATA

2.1. Hubble Space Telescope

SPT-0356 was observed in 2021 as part of a joint Chandra-HST program (Chandra Proposal ID #22800530, 79 ks; HST-GO-16425, 8 orbits, PI: Mahler) with a primary goal to determine whether SPT-0356 is a dissociated major merger by constraining the hot gas from X-ray and the dark matter potential from gravitational lensing in the optical. We obtained two orbits of HST imaging with the Wide Field Camera 3 (WFC3) on 2021 March 6. Each orbit was split between F110W and F160W, resulting with a total of 2422 s in WFC3-IR/F110W and 2622 s in WFC3-IR/F160W. We obtained six orbits of HST imaging with the Advanced Camera for Surveys (ACS) on 2021 May 8-9, with ACS/F606W and ACS/F814W. The ACS observations are a mosaic of three overlapping pointings to achieve a wide field of view and maximal depth at the center. Each pointing was observed for two orbits, and each orbit split between the two filters, reserving the darker half of the orbit (less Earthshine) for F606W. At the core of the cluster (and the strong lensing region),

the ACS mosaic achieved a three-orbit depth (10,584 s total) in each of F814W and F606W. To the new observations we co-added one frame of archival ACS/F606W imaging obtained on 2014 June 25 as part of GO-13412 (PI: Schrabback), with exposure time of 2320 s.

The HST data (DOIs: 10.17909/9mak-cy86 ; Titled: HST imaging data for SPT-CL-J0356-5337) were reduced using standard procedures with `Drizzlepac`¹. Sub-exposures taken with each filter were combined with `astrodrizzle`, using a Gaussian kernel with a drop size `finalpixfrac=0.8`. Images from different visits were aligned using `tweakreg` and `tweakback` for a WCS- and pixel-frame matched mosaic, with a pixel scale of $0''.03$ per pixel. [Figure 1](#) shows the field of view covered with HST. The ACS data cover a field out to $\sim 2''.7$ from the cluster center, intended to facilitate weak lensing analysis. The WFC3 data were not tiled, and cover only the cluster core.

2.2. MUSE

We observed the core of SPT-0356 with the Multi-Unit Spectrograph Explorer (MUSE; [Bacon et al. 2010](#)) on VLT (ESO project 106.21JF.001, PI: Mahler). The observations were taken between 2021 Jan 16 and 2021 Feb 20 for a total exposure time of 14.04 ks over four different Observing Blocks, at grey time, with a reported seeing of $0''.8$. They were centered on R.A., Decl. = $[03:56:21.512; -53:37:51.954]$, to maximize the strong lensing region coverage.

The MUSE data were reduced with the European Southern Observatory (ESO) pipeline using MPDAF version 3.5 and ZAP version 2.1 ([Weilbacher 2015](#)) and then reprocessed to improve flat fielding and sky subtraction using a dedicated pipeline together with MPDAF tools ([Bacon et al. 2016](#)), following a methodology similar to the one described in [Fumagalli et al. \(2016, 2017\)](#). We refer the reader to these papers for more details and only give a brief summary of the post-processing steps here: (1) the individual exposures were resampled to a common astrometric grid defined by the final ESO reduction; (2) a correction of imperfections in the flat fields was applied using the MPDAF self-calibration method as described in [Bacon et al. \(2017\)](#), and sky subtraction was performed with the ZAP tool, which uses principal-component analysis ([Soto et al. 2016](#)); and (3) individual exposures were combined to obtain a single data cube using an average 3σ clipping algorithm. Finally, we aligned the reduced cube to the HST images.

¹ <http://www.stsci.edu/scientific-community/software/drizzlepac.html>

We extracted spectra from the MUSE data following a similar procedure as [Mahler et al. \(2018\)](#). Spectra were extracted following a mask based on the continuum F814W HST bands segmentation map, convolved with a $0''.8$ FWHM to mimic the effect of the seeing. The redshift identification follows the same classification as [Mahler et al. \(2018\)](#) with maximum confidence, confidence 3, assigned to objects with several, clearly identified, emission or absorption lines; confidence 2 redshift identifications rely on one emission line (e.g., H α , narrow Ly α) or a few faint absorption lines (e.g., low signal-to-noise balmer lines); confidence 1 redshifts are tentative identification and are unreliable but are still recorded. The final catalog contains spectra from 153 sources, of which 32 are classified as cluster member galaxies (see [Section 4.2](#)) and five were identified as multiply-imaged systems ([Figure 2](#)). The spectroscopic redshifts of multiple images used in this work are listed in [Table 1](#) and further discussed in [Section 3.1](#). The rest of the catalog will be published in a later study.

2.2.1. Spectroscopic redshifts of Cluster-Member Galaxies

The MUSE field of view is centered on the BCG, and provides spectroscopic redshifts of galaxies out to $\sim 41''$ from the BCG. This includes the group of luminous red galaxies (LRGs) projected $\sim 21''$ west of the BCG, which we refer to as the “LRGs core” or “LRGs sub-cluster” in this paper. The redshift distribution of the 32 cluster-members within the MUSE field of view confirms the findings of [Mahler et al. \(2020\)](#), that the two main cores of SPT-0356, the “BCG core” and the “LRGs core”, are at the same redshift. Quantitatively, a tight group of seven galaxies in the “LRGs core” have an average velocity offset from the BCG core of just a few km s^{-1} (median 135 km s^{-1}). We take the redshift of the cluster as the median of 21 galaxies in the cluster core between $1.03 < z < 1.04$, $z_{cluster} = 1.034$. An elaborate dynamical investigation of this cluster will be presented in a forthcoming publication ([Mahler et al., in prep.](#)).

3. LENSED SOURCES

3.1. Identification of Multiple Images

[Mahler et al. \(2020\)](#) identified and spectroscopically confirmed three multiply-imaged lensed sources — all with images appearing between the two sub-halos of the cluster. The spectroscopic identification was part of the follow-up campaign within the SPT collaboration using Magellan/LDSS3, Magellan/FIRE, and Gemini/GMOS-South spectrograph. Each source has three images, for a total of nine. They used the single-

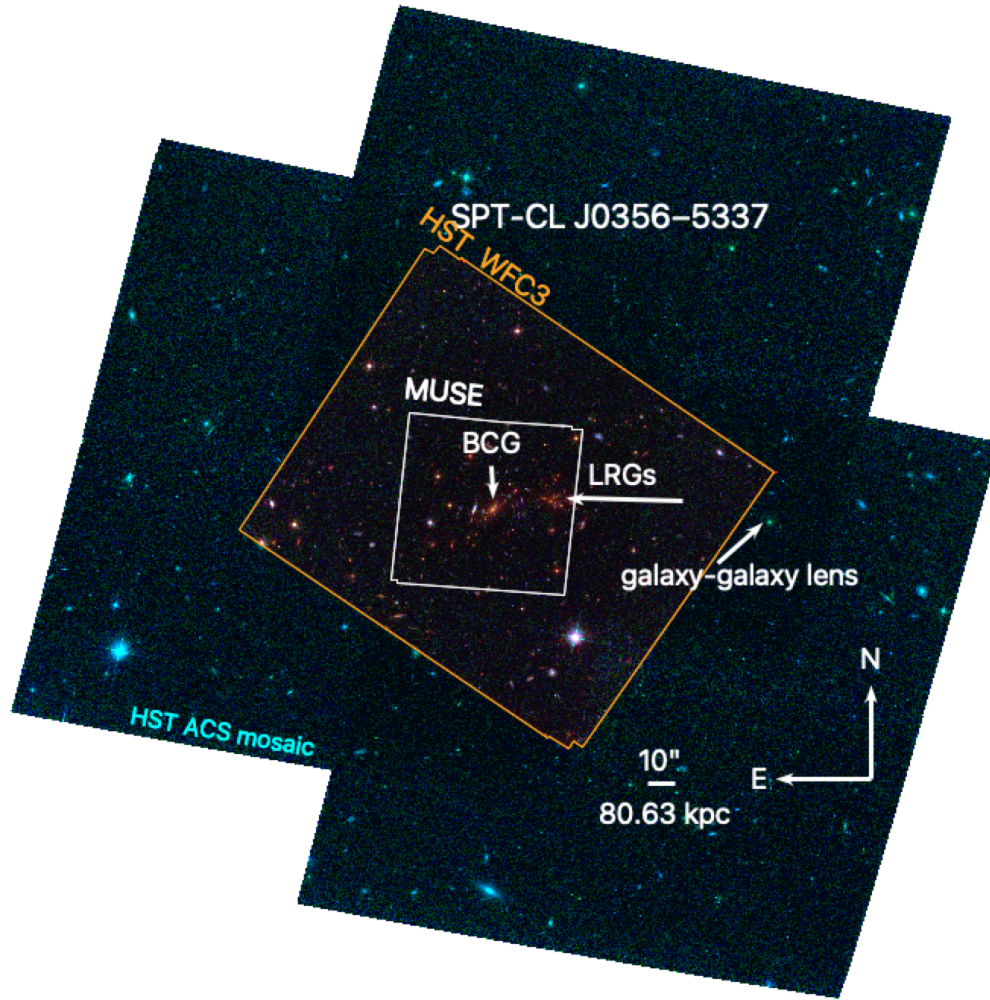


Figure 1. HST imaging of SPT-0356 using WFC3/F160W (red), ACS/F814W (green) and ACS/F606W (blue). Cluster components are labeled in white. The different instrument footprints are labeled in white (MUSE), orange (HST WFC3), and cyan (HST ACS mosaic).

band HST imaging that was available at the time to use the substructure of each source as individual constraint, multiplexing two of the systems into three sets of constraints each. We adopt the ID scheme of Mahler et al. (2020) for consistency; these systems are identified as system 1, source 2, and source 3. The latter was confirmed again with MUSE spectroscopic data using the Ly α line, other systems were in the so-called *redshift desert* and did not yield any confirmation. For system 3, we kept the redshift estimated from [OIII] as reported in Mahler et al. (2020) as it is a better tracer than Ly α of the systemic redshift.

Using the new HST data, we confirmed the identification of the three secure lensed sources in Mahler et al. (2020) and identified additional lensed galaxies in new, previously unconstrained areas of the field. To the west of the LRGs, we identified system 4, with two distinct

emission knots, creating families 4 and 41. We extracted a redshift of $z = 3.0205$ for this system from the MUSE data, from a Ly α emission line (see Section 3.2).

To the east of the BCG, we considered as candidate families 5, 7 and 8. Family 7 appears as three images $\sim 18''$ southeast of the BCG. The HST colors as well as the wide separation of $24''.5$ between 7.1 and 7.3 point to a lensed source at a relatively high redshift. We spectroscopically confirmed family 7 using the MUSE data at $z = 5.3288$, from a Ly α emission line (see Section 3.2). Family 5 appears as three faint images with similar colors, and geometry consistent with the lensing expectation. However, since we were unable to confirm this source with MUSE, it remains a candidate and was not used as a constraint in the lens model. The lens model places this system at $z \sim 2.34$. Candidate 8, at R.A., Decl. = [59.1011420, -53.6342524], was con-

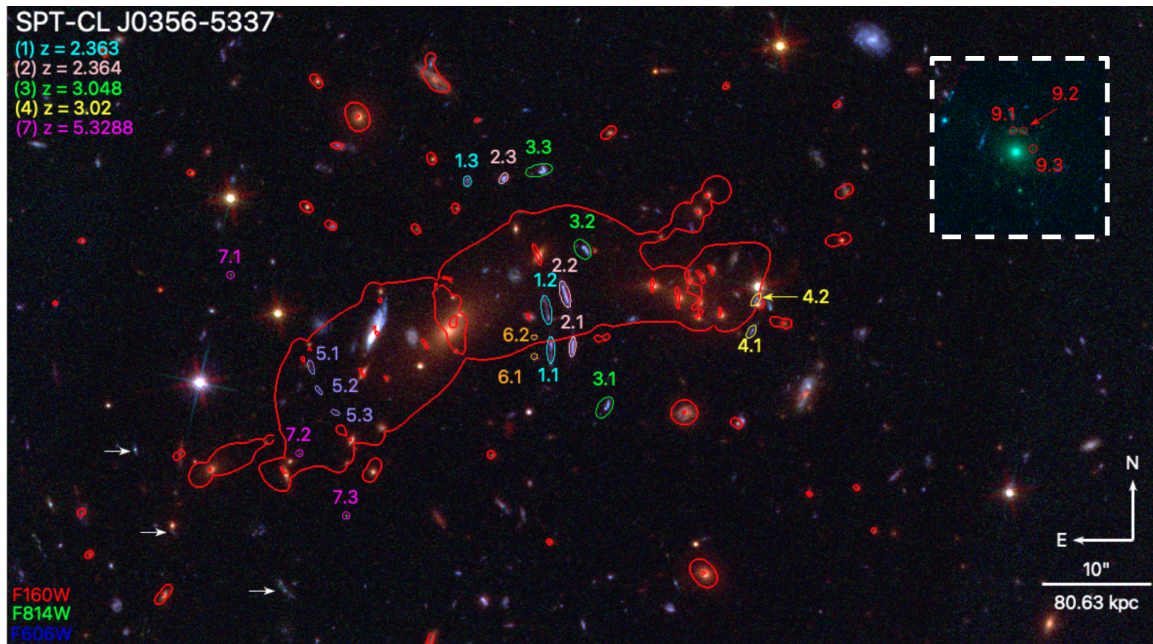


Figure 2. HST image of SPT-0356 with lens model constraints labeled. The critical curve at $z = 3$ is shown for model B. Arcs and arc candidates are labeled and color-coded by system; their coordinates are listed in Table 1. White arrows point to the LAEs discussed in Section 3.2. An inset shows a galaxy-galaxy lens found $101''.1$ west of the BCG (see Section 3.1 and Figure 1), at the same scale. The area containing the galaxy-galaxy lens is only covered by ACS, and is missing the WFC3-IR filters.

sidered because of its arc-like morphology, however, it was not confirmed as a lensed source: the orientation and lack of obvious counter images make it an unlikely multiply-imaged lensed source that could form a useful constraint. We were not able to determine the redshift of this galaxy from MUSE; its colors are consistent with the cluster red sequence. This galaxy was left out of the analysis.

Between the two cluster cores, we identified candidate system 6 between the BCG and system 1. It has two arcs straddling the critical curve near 1.2 and 1.3, with blue emission and a lensing geometry similar to that of system 1. No obvious redshift was found in the MUSE data for this family, and given its proximity to system 1 we did not use it to constrain the model despite it being a high-confidence candidate. The model predicts $z \sim 3.13$, and a third image ~ 2 mag fainter $\sim 17''$ north of the BCG, where several faint blue sources can be observed. Finally, we identified a star forming clump near each of the images of system 3, with similar lensing configuration. We label this family as system 33. As the Ly α emission encompasses a wide region around the HST-identified clumps (see Section 3.2), we could not extract a unique spectroscopic redshift for this knot to definitively determine whether it is part of source 3. We therefore left its redshift as a free parameter. The lens model-predicted redshift of this source is in agreement with that of source 3.

We also identified galaxy-galaxy lensing evidence appearing as a partial Einstein ring around an elliptical galaxy, located $101''.1$ west of the BCG (system 9; see inset in Figure 2). We do not have full color data in this area and we were unable to obtain a spectroscopic redshift for the arc, as it is outside of both the WFC3 and MUSE footprints. This arc was not used as a modeling constraint in the final model (see Section 4.3 for discussion).

A likely background group of three Ly α emitting galaxies at $z = 4.1448$ was also considered as candidate multiply-imaged system, and ruled out. We describe this group in Section 3.2.

We examined and ruled out the three *candidate multiply imaged system* proposed by Mahler et al. (2020, Table 3), based on the inconsistent HST colors and morphology or MUSE spectroscopy. Our candidate image 5.2c coincides with one of the candidates of Mahler et al. (2020, candidate 5.2), however with different candidate counter images. Candidate System 6 in Mahler et al. (2020) coincides with one of the LAE galaxies at 4.1448 discussed in Section 3.2, and is not multiply imaged.

Table 1 lists the ID, coordinates, and redshifts of the identified images of lensed sources and candidates. The images are labeled as A.X where A is a number indicating the lensed source ID and X indicates a specific lensed image of source A. For example, source 7 is visible as three lensed images: 7.1, 7.2, and 7.3. We can in-

ID	R.A. [J2000]	Decl. [J2000]	z	rms ["]	μ_{median}	μ_{best}
1.1	59.0852022	-53.6314475	2.363	0.22	$8.5^{+3.1}_{-1.5}$	8.5
1.2	59.0853168	-53.6307905	2.363	0.03	$6.1^{+2.0}_{-1.2}$	6.0
1.3	59.0887924	-53.6272615	2.363	0.30	$2.5^{+0.6}_{-0.3}$	2.5
11.1	59.0852061	-53.6317905	2.363	0.38	$4.9^{+1.6}_{-0.7}$	5.0
11.2	59.0855040	-53.6303465	2.363	0.30	$5.7^{+3.5}_{-1.3}$	6.0
11.3	59.0887949	-53.6273977	2.363	0.36	$2.7^{+0.7}_{-0.3}$	2.6
2.1	59.0843011	-53.6316673	2.364	0.13	$4.7^{+1.5}_{-0.6}$	4.7
2.2	59.0846952	-53.6300065	2.364	0.09	$6.7^{+4.8}_{-1.6}$	7.2
2.3	59.0872684	-53.6272840	2.364	0.12	$2.9^{+0.7}_{-0.4}$	2.9
21.1	59.0842829	-53.6315221	2.364	0.05	$5.6^{+1.9}_{-0.8}$	5.6
21.2	59.0846032	-53.6301888	2.364	0.08	$7.3^{+4.7}_{-1.7}$	7.8
22.1	59.0842691	-53.6314058	2.364	0.09	$6.7^{+2.3}_{-1.1}$	6.7
22.2	59.0845130	-53.6303539	2.364	0.14	$8.5^{+4.8}_{-1.9}$	9.1
3.1	59.0828569	-53.6331037	3.048	0.13	$2.5^{+0.9}_{-0.3}$	2.6
3.2	59.0838084	-53.6289998	3.048	0.04	$3.2^{+1.0}_{-0.6}$	3.1
3.3	59.0856499	-53.6270832	3.048	0.13	$4.4^{+1.7}_{-0.8}$	4.2
31.1	59.0827714	-53.6330331	3.048	0.12	$2.6^{+0.9}_{-0.3}$	2.6
31.2	59.0836965	-53.6290506	3.048	0.02	$2.7^{+0.9}_{-0.5}$	2.5
31.3	59.0855083	-53.6270606	3.048	0.14	$4.4^{+1.7}_{-0.8}$	4.2
32.1	59.0827509	-53.6329767	3.048	0.15	$2.6^{+0.9}_{-0.3}$	2.6
32.2	59.0836564	-53.6291151	3.048	0.02	$2.3^{+0.8}_{-0.4}$	2.1
32.3	59.0855392	-53.6269909	3.048	0.14	$4.1^{+1.5}_{-0.7}$	4.0
33.1	59.0831075	-53.6332247	$3.06^{+0.12}_{-0.11}$	0.05	$2.5^{+0.8}_{-0.3}$	2.5
33.2	59.0840906	-53.6289688	$3.06^{+0.12}_{-0.11}$	0.08	$3.1^{+1.1}_{-0.6}$	3.0
33.3	59.0860422	-53.6271129	$3.06^{+0.12}_{-0.11}$	0.20	$4.2^{+1.5}_{-0.7}$	4.1
4.1	59.0765359	-53.6311011	3.0205	0.08	$7.2^{+6.3}_{-2.9}$	8.4
4.2	59.0764350	-53.6303685	3.0205	0.07	$11.3^{+20.6}_{-8.1}$	16.6
4.3c	59.0766660	-53.6291637	3.0205	...	$12.3^{+167.7}_{-5.6}$	25.3
41.1	59.0766346	-53.6311878	3.0205	0.29	$6.3^{+4.4}_{-2.3}$	7.0
41.2	59.0763229	-53.6302903	3.0205	0.15	$14.5^{+159.9}_{-9.9}$	82.8
41.3c	59.0765992	-53.6292369	3.0205	...	$12.0^{+152.3}_{-5.5}$	22.2
5.1c	59.0954663	-53.6321227	~ 2.34	...	48^{+1000}_{-33}	32
5.2c	59.0952147	-53.6326267	~ 2.34	...	30^{+680}_{-21}	136
5.3c	59.0944939	-53.6332017	~ 2.34	...	40^{+940}_{-28}	58
6.1c	59.0859156	-53.6317767	$3.13^{+0.33}_{-0.25}$...	$3.3^{+1.2}_{-0.5}$	3.2
6.2c	59.0859224	-53.6312904	$3.13^{+0.33}_{-0.25}$...	$18.5^{+7.7}_{-5.6}$	19.1
7.1	59.0989640	-53.6297059	5.3288	0.05	$2.8^{+1.3}_{-0.4}$	2.9
7.2	59.0960027	-53.6342447	5.3288	0.10	$1.5^{+0.6}_{-0.2}$	1.4
7.3	59.0939978	-53.6358341	5.3288	0.13	$3.9^{+1.2}_{-0.6}$	4.0
9.1c	59.0423509	-53.6318281
9.2c	59.0418968	-53.6318360
9.3c	59.0414829	-53.6323020

Table 1. Lensing constraints and candidate lensed systems. ID refers to the name of each lensed image. A ‘c’ after the image ID denotes that the image is a candidate and was not used as a constraint in the model. The “ z ” column tabulates the redshift of each source. Redshifts without error bars are spectroscopically confirmed and were used as hard constraints in the model, while those with error bars are model predictions. The spectroscopic redshift of sources 1, 2, and 3 are from [Mahler et al. \(2020\)](#). The redshift of system 33 was included in the optimization as a free parameter. The spectroscopic redshifts for sources 4 and 7 were found from the spectral analysis of the MUSE cube (see [Section 3.1](#)). For candidate 5, the model-predicted redshift is uncertain and represents a redshift for which the model produces multiple images at this location, also resulting in a poorly-constrained high magnification. The redshift of candidate 6 is estimated from the best fit parameters of model B. “rms” represents the scatter in the image plane between the predicted and observed images of each source. The last two columns list the magnification measured at the location of the listed coordinates, with 95% confidence uncertainties measured from Model B ([Table 2](#)). μ_{median} is the median from the full MCMC chain; μ_{best} is measured from the best-fit model.

crease the number of constraints by mapping individual star forming clumps within each image to their counter-images. In this case, we label them as AB.X, where B refers to a single emission knot in system A. For example, system 3 has three distinct emission knots. We refer to these as 31, 32, and 33. Each of these are imaged multiple times, leading to, e.g., 31.1, 31.2, 31.3. For all constraints used in this lensing analysis, as well as arc candidates, see Figure 2 and Table 1.

3.2. Detection of Extended Ly α Emission from Background Galaxies

Our MUSE observations (see Section 3.1) revealed extended Ly α emission associated with several background sources. System 7 was identified in the MUSE data as a new strongly-lensed system, with three images of a Ly α -emitting (LAE) galaxy, presenting compact Ly α emission at $z = 5.3288$, with matching optical counterparts in the HST imaging. System 3 (at $z = 3.048$) and System 4 (at $z = 3.0205$) present large diffuse Ly α nebulae where the peaks of the emission are clearly offset from the HST continuum emission. The Ly α emission from sources 4, 3, and 7 is shown as contours on top of the HST image in Figure 3. The magnifications of these arcs are listed in Table 1.

In addition to the secure strongly-lensed LAEs, we have identified double-peaked Ly α emission at $z = 4.1448$ from three sources in the eastern outskirts of the strong lensing regime. Figure 4 shows the Ly α contours overplotted on the HST imaging (left panel), and the double-peaked Ly α line of the three galaxies (right panel). There is no evidence of other nebular lines such as CIV, SiII, FeII, CIII] etc. in the spectra. The redshift is assumed from the red Ly α peak, which is observed at 6254.35\AA . The blue peak is observed at 6243.80\AA . The spatial geometry of the Ly α emission suggests a multiply-imaged system. However, further examination of this emission leads us to conclude that these are likely not three images of the same galaxy, and may instead be a small background group at $z = 4.1448$. First, all three Ly α detections have an associated optical continuum counterpart in the HST imaging, however, with strikingly different morphology, and inconsistent optical colors and surface brightnesses. Second, while the LAE spectra show very similar redshifts, their blue-to-total flux ratios are dissimilar among the three galaxies. Finally, the lensing configuration is inconsistent with the constraint on the lensing potential placed by the nearby high-confidence System 7. Ray-tracing the three sources through the lens model to their source redshift $z = 4.1448$, we find that two of the galaxies are separated by approximately 14 kpc in projection, with

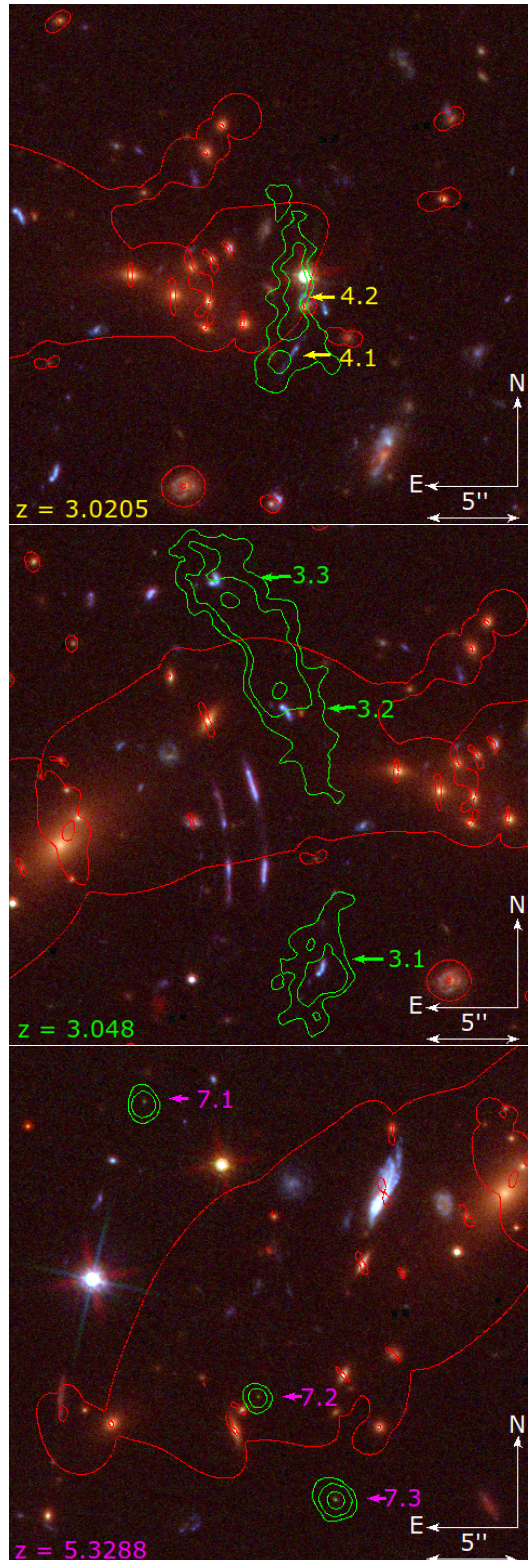


Figure 3. Zoom-in on three strongly-lensed galaxies with multiple images, showing Ly α emission in MUSE IFU. The Ly α emission is represented with green contours overlaid on the HST imaging. The top two systems show extended Ly α emission with peaked emission offset from the HST continuum. The bottom row shows three images of a very compact Ly α emitter. Contour levels are at 250, 500, 2500, and $5000 \times 10^{-20} \text{ ergs s}^{-1} \text{ cm}^{-2} \text{ arcsec}^{-2}$. The critical curve from the best-fit model is overplotted in red in each panel, at the redshift of the emitter.

the third approximately 40 kpc away. [Figure 5](#) shows a reconstruction of the $z = 4.1448$ source plane, done by ray-tracing the three LAEs through the best-fit lens model. We note that choosing a systemic redshift based on the bluer peak or central wavelength has insignificant implication to the lensing interpretation. The magnification of these three LAEs are: $\mu_{med} = 3.9 \pm 0.6$ for the northern galaxy, $\mu_{med} = 3.7 \pm 0.5$ for the middle galaxy, and $\mu_{med} = 2.0 \pm 0.3$ for the southern galaxy, all estimated from our fiducial lens model (model B, see [Section 4.3](#)). An investigation of the circumgalactic gas surrounding this group is beyond the scope of this paper.

4. LENSING ANALYSIS

4.1. Methodology

We modeled the cluster using the publicly available parametric lens modeling algorithm `Lenstool` ([Jullo et al. 2007](#)). `Lenstool` uses Markov Chain Monte Carlo (MCMC) formalism to explore the parameter space and identify the set of parameters that produce the smallest scatter between observed and predicted strong lensing constraints. As constraints for the lens model, we used the positions of multiple images of lensed sources ([Section 3.1](#)) as well as their spectroscopic redshifts when available. `Lenstool` creates models that are linear combinations of galaxy- and cluster-scale halos. In this analysis, all halos were represented with the pseudo-isothermal ellipsoidal mass distribution (dPIE, also referred to in the literature as PIEMD), which has seven parameters: position (x, y) , ellipticity e , position angle θ , core radius r_{core} , truncation radius r_{cut} , and normalization σ_0 . For cluster-scale halos, we fixed r_{cut} at 1500 kpc, since this parameter is far outside the strong lensing region where lensing constraints are observed; we allowed all other parameters to be optimized by `Lenstool`, unless otherwise noted. For galaxy-scale halos, the positional parameters (x, y, e, θ) were fixed to the observed positions of their respective cluster member galaxies, as measured with `Source Extractor` ([Bertin & Arnouts 1996](#)), and the other parameters scaled to their magnitudes through scaling relations ([Jullo et al. 2007](#)) as an ensemble adding only two free parameters to the optimization process.

Our starting point for the lens model is the model published by [Mahler et al. \(2020\)](#). With the multi-band HST data and this preliminary lens model, we secured four new lensed sources and measured the redshifts of two of these using MUSE data (see [Section 3.1](#)). We then converged on the best lens model by iteratively adding complexity to the model. The final lens model has positional constraints from 32 multiple images of

five spectroscopically confirmed lensed sources and substructure within them.

4.2. Selection of Cluster Galaxies

Cluster member galaxies were selected photometrically and spectroscopically. We generated a photometric catalog of extended sources (galaxies) in the HST/WFC3 field of view using `Source Extractor` ([Bertin & Arnouts 1996](#)) in dual-image mode with the F110W image as the detection image, and magnitudes measured within the same apertures in F110W and F160W. We then matched the photometric catalog with the MUSE spectroscopic redshift list by coordinates. [Figure 6](#) shows the F110W–F160W vs. F110W color-magnitude diagram of galaxies in this field of view. Galaxies with spectroscopic redshifts in the range $1.015 < z < 1.055$, overplotted in green, highlight the cluster red sequence ([Gladders & Yee 2000](#)). We fit the 32 spectroscopically-confirmed cluster members in the MUSE field of view with a linear fit, using iterative $3\text{-}\sigma$ clipping, to define the red sequence and its width in color-magnitude space. We then applied the red sequence selection (solid line in [Figure 6](#)) to the full photometric catalog, to expand the selection to galaxies as faint as F110W=27.5 mag and galaxies outside the MUSE field of view. The final catalog has a total of 149 cluster member galaxies.

4.3. Mass Halos

Our lens model describes the lens plane as a linear combination of cluster-scale halos and galaxy-scale halos ([Figure 7](#)). The cluster-member distribution motivates at least two cluster components. We explored the possibility of a more or less complex mass distribution by allowing a third cluster-scale halo or removing the second cluster-scale halo. This is further discussed in [Section 6](#). As noted above, all the halos are parameterized as dPIE. Halo 1 (H1) is a cluster-scale dark matter halo associated with the BCG sub-cluster. H2 is a cluster-scale dark matter halo associated with the LRGs sub-cluster. All the parameters of these two halos were allowed to vary, with the exception of r_{cut} as explained in [Section 4.1](#). H3 is a galaxy-scale halo, centered on a galaxy observed near the images of system 4; we freed the slope and normalization parameters of this galaxy, to better account for small disturbances in the lensing potential in this region, while keeping x , y , e , and θ fixed to their observed properties as measured by `Source Extractor`. H4 was added to the model east of system 7, to explore whether additional mass in that region was needed in order to reproduce the lensing evidence and the apparent high ellipticity of the lens. All

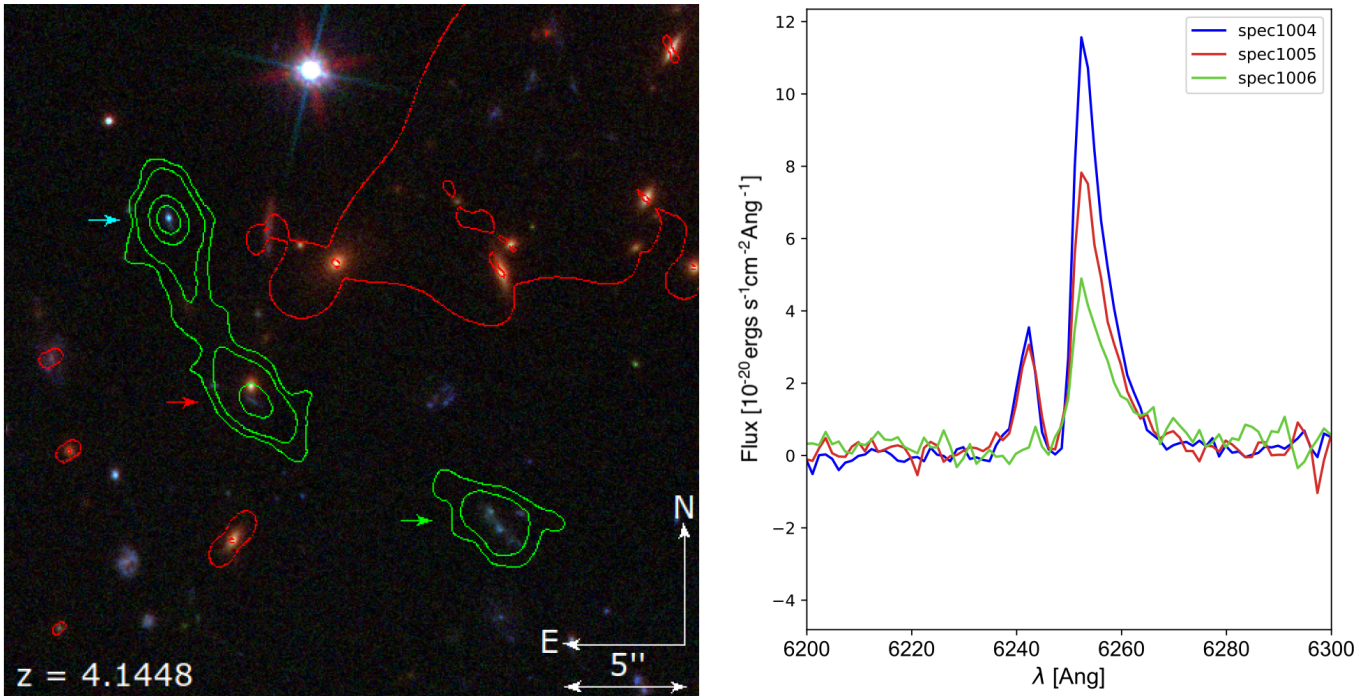


Figure 4. *Left:* HST imaging and Ly α contours of three LAEs $\sim 30''$ southeast of the BCG. Contours of the Ly α levels from MUSE are plotted at $250, 500, 2500,$ and $5000 \times 10^{-20} \text{ ergs s}^{-1} \text{ cm}^{-2} \text{ arcsec}^{-2}$. The critical curve for the redshift of these galaxies is overplotted in solid red line. *Right:* The extracted spectra of the three sources shown in line colors that match the three arrows in the left panel. The double peak emission is observed at 6254.35 \AA and 6254.35 \AA . The redshift of $z = 4.1448$ is measured from the redder Ly α peak. Although these three galaxies are at the same redshift, the spectroscopy and imaging data, as well as the lensing analysis, indicate that they are most likely not multiple images of the same source.

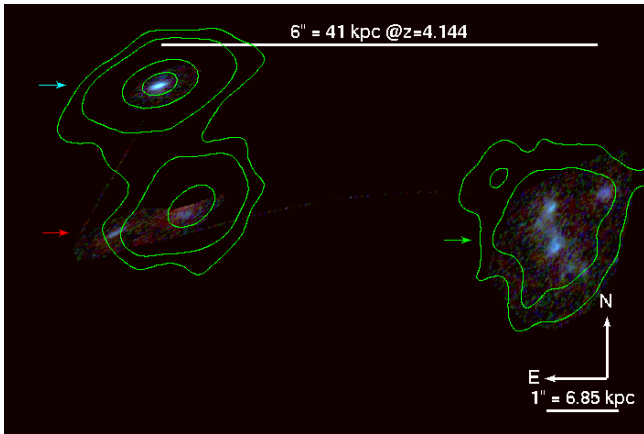


Figure 5. The three LAEs at $z = 4.1448$, raytraced to the sourceplane (Ly α contours from MUSE overplotted on the HST imaging). The galaxies are separated by $\sim 40 \text{ kpc}$ when unlensed, and likely form a small background group.

the parameters of this halo were allowed to vary within broad priors.

H5 is a galaxy-scale halo that accounts for the mass of the “jellyfish” galaxy (Mahler et al. 2020), a bright infalling star-forming cluster member galaxy $7''$ east of the BCG. This galaxy was not included in the cluster-member catalog, as it does not follow the same mass-

luminosity relation as quiescent cluster member galaxies. Using the same mass-luminosity relation would have assigned too much mass to this galaxy – the jellyfish galaxy is apparently star-forming, and is therefore brighter than a similarly-massive elliptical galaxy would be. We included this halo in the model as an independent galaxy-scale halo decoupled from the scaling relations of typical cluster members, restricting its parameters so that its mass would remain consistent with a cluster-member galaxy at this redshift.

In some iterations of the lens model, we freed the galaxy-galaxy lens halo (observed $101''1$ west of the cluster core), allowing its parameters to be constrained by system 9 (shown in the inset in Figure 2). Freeing the galaxy-scale halo had no detectable effect on the model, so we ultimately left this galaxy linked to the other galaxies in the galaxy catalog. Consequently, system 9 was not used to constrain the cluster lens model. We also investigated whether the BCG should be decoupled from the mass-luminosity relation of the rest of the cluster-member galaxies, by freeing the normalization and slope parameters of the BCG (σ_0, r_c, r_{cut}). In all the tested cases, the models converged on similar results as models with these three parameters linked to the scaling relations, and did not produce better rms or

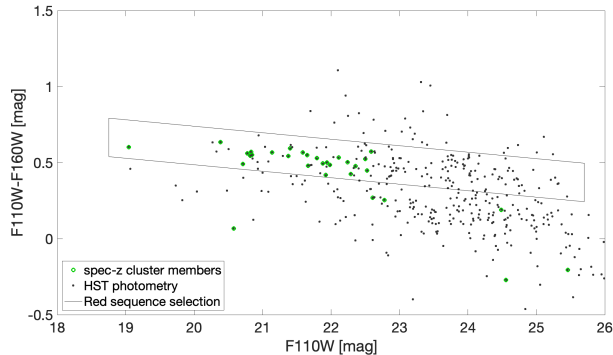


Figure 6. Color-magnitude diagram of galaxies in the HST/WFC3 field of view. The F110W-F160W color is plotted against F110W magnitude. Cluster member galaxies form a red sequence in this parameter space, highlighted by spectroscopically-selected cluster members (green data-points). The solid line marks the cluster member selection, based on a linear fit to the spectroscopically-selected members.

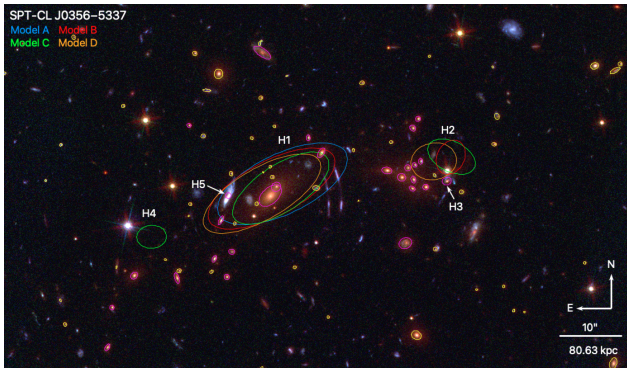


Figure 7. Image of the field with cluster member galaxies identified. Magenta ellipses denote cluster member galaxies spectroscopically confirmed using MUSE data. Yellow ellipses denote cluster member galaxies identified by color (see Section 4.2). The dark matter halos described in Section 4.3 are identified in blue, red, green, and orange for models A, B, C, and D, respectively.

χ^2 . Our models therefore treat the BCG the same as the rest of the cluster members.

In total, the models have 149 galaxy scale halos, and 1-3 cluster-scale halos.

5. RESULTS

The multi-band HST imaging and MUSE spectroscopy resulted in the robust identification of lensing constraints in previously-underconstrained areas of the lens. Improving upon the previous model, the mass distribution is now better constrained in the center, and, most importantly, east of the BCG and west of the LRGs.

As described above, the iterative process of converging on the best description of the lens plane that satisfies the lensing constraints starts with a simple model and gradually increases the complexity until new models do not significantly improve the goodness of fit. We investigated several lens models with increasing complexity level and number of free parameters, spanning a range of modeling choices. Model A, with the least number of constraints, describes the lens plane with one cluster-scale halo (H1) plus cluster-member galaxies. Model B adds a second halo (H2) near the group of LRGs. Model C adds a third halo (H4) in the east part of the cluster. We also present results from models D and E, which are similar to model B and C, respectively, except that the scaling relations of cluster-member galaxies are fixed, limiting the galaxy contribution to about 10% of the total cluster mass.

The parameters of the five models are tabulated in Table 2. Statistical uncertainties on the best-fit model parameters were obtained from the MCMC sampling of the parameter space, and represent a 95% confidence interval. Parameters that were not optimized are listed with square brackets.

To assess the lens models we evaluated two criteria: the image-plane rms and the Bayesian information criterion (BIC). The rms is the average image-plane scatter between the observed positions of lensed images and their positions predicted by the model. A model is generally considered better if it has a lower rms. According to this criterion, the favored lens model is the one with the highest flexibility, Model C, which allows three cluster-scale halos (H1, H2, and H4), and solves for the normalization of the cluster-members’ scaling relation as free parameters. This model achieved image plane rms of $0''.14$.

The second criterion, BIC, provides a quantitative method of comparing similar models by penalizing a higher number of free parameters, which helps to prevent overfitting. The BIC is calculated using the following equation (Schwarz 1978):

$$BIC = -2 \ln(\mathcal{L}) + k \ln(n), \quad (1)$$

where \mathcal{L} is the likelihood, k is the number of free parameters, and n is the sample size, which is chosen to be the number of constraints, $n = [2 \times \text{the number of multiple images} - 2 \times \text{the number of sources}]$ (see Lorah & Womack 2019 for a discussion of the difference between the sample size and the number of constraints). A model with lower BIC is considered to be statistically preferred.

The BIC values are listed in Table 2. We find that the BIC increases with the number of parameters. Although models with higher complexity result in better recovery

Model	Halo	Δ R.A. ["]	Δ Decl. ["]	e	θ [deg]	σ_0 [km s ⁻¹]	r_{cut} [kpc]	r_c [kpc]
A: H1	H1	$-2.05^{+0.85}_{-0.93}$	$1.94^{+0.47}_{-0.51}$	$0.74^{+0.06}_{-0.10}$	$25.4^{+1.4}_{-1.1}$	939^{+44}_{-46}	[1500]	82^{+10}_{-12}
one cluster halo	H3	[-28.31]	[2.34]	[0.18]	[19.08]	93^{+95}_{-15}	20^{+74}_{-19}	$0.06^{+0.43}_{-0.04}$
rms=0''20, $\chi^2 = 14.03$, k=15	H5	[6.69]	[-0.03]	[0]	[0]	80^{+164}_{-24}	29^{+19}_{-27}	$0.03^{+0.06}_{-0.03}$
$\ln(\mathcal{L}) = 11.23$, BIC=32.9	L*	$247.7^{+1.5}_{-35.5}$	53^{+25}_{-11}	[0.15]
B: H1+H2	H1	$-0.20^{+2.95}_{-0.88}$	$1.12^{+0.68}_{-1.57}$	$0.73^{+0.07}_{-0.12}$	$27.4^{+2.8}_{-2.8}$	884^{+30}_{-166}	[1500]	68^{+10}_{-27}
two cluster halos	H2	$-28.9^{+13.6}_{-1.6}$	$6.2^{+3.6}_{-3.9}$	$0.26^{+0.60}_{-0.23}$	243^{+30}_{-137}	373^{+186}_{-20}	[1500]	37^{+62}_{-11}
rms=0''17, $\chi^2 = 9.89$, k=21	H3	[-28.31]	[2.34]	[0.18]	[19.08]	51^{+142}_{-13}	81^{+16}_{-80}	$0.15^{+0.33}_{-0.14}$
$\ln(\mathcal{L}) = 13.3$, BIC=50.9	H5	[6.69]	[-0.03]	[0]	[0]	150^{+95}_{-96}	14^{+35}_{-12}	$0.01^{+0.08}_{-0.01}$
	L*	$246.5^{+2.7}_{-51.5}$	$43.1^{+34.7}_{-6.8}$	[0.15]
C: H1+H2+H4	H1	$-1.7^{+2.6}_{-1.3}$	$1.2^{+1.0}_{-1.3}$	$0.70^{+0.10}_{-0.15}$	$33.1^{+7.2}_{-6.6}$	739^{+141}_{-200}	[1500]	44^{+25}_{-27}
three cluster halos	H2	$-29.1^{+13.8}_{-1.8}$	$6.3^{+1.9}_{-2.1}$	$0.48^{+0.36}_{-0.42}$	154^{+104}_{-38}	448^{+183}_{-86}	[1500]	$24.4^{+72.5}_{-3.2}$
rms=0''14, $\chi^2 = 6.91$, k=28	H3	[-28.31]	[2.34]	[0.18]	[19.08]	$40.2^{+67.2}_{-9.2}$	88^{+10}_{-85}	$0.28^{+0.21}_{-0.27}$
$\ln(\mathcal{L}) = 14.79$, BIC=73.7	H4	$19.0^{+10.6}_{-4.4}$	$-6.6^{+1.4}_{-6.6}$	$0.26^{+0.02}_{-0.24}$	$3.48^{+173.61}_{-0.91}$	312^{+182}_{-195}	348^{+624}_{-206}	$16.6^{+66.4}_{-5.5}$
	H5	[6.69]	[-0.03]	[0]	[0]	81^{+163}_{-24}	$12.1^{+36.7}_{-9.6}$	$0.07^{+0.03}_{-0.06}$
	L*	231^{+17}_{-41}	62^{+16}_{-28}	[0.15]
D: fixed galaxies (1)	H1	$1.3^{+1.8}_{-1.8}$	$0.3^{+1.0}_{-1.3}$	$0.74^{+0.05}_{-0.21}$	$29.8^{+2.1}_{-3.4}$	823^{+89}_{-82}	[1500]	47^{+21}_{-18}
H1+H2	H2	$-26.2^{+10.5}_{-2.8}$	$5.5^{+2.4}_{-2.5}$	$0.22^{+0.22}_{-0.21}$	190^{+81}_{-82}	494^{+109}_{-134}	[1500]	43^{+34}_{-18}
rms=0''17, $\chi^2 = 10.62$, k=19	H3	[-28.31]	[2.34]	[0.18]	[19.08]	55^{+124}_{-14}	$88.8^{+5.8}_{-86.8}$	$0.34^{+0.15}_{-0.33}$
$\ln(\mathcal{L}) = 12.93$, BIC=44.2	H5	[6.69]	[-0.03]	[0]	[0]	123^{+121}_{-69}	$6.8^{+41.8}_{-4.1}$	$0.07^{+0.03}_{-0.06}$
	L*	[217]	[39]	[0.15]
E: fixed galaxies (2)	H1	$0.2^{+2.1}_{-2.5}$	$0.5^{+1.7}_{-1.3}$	$0.65^{+0.14}_{-0.10}$	$33.4^{+0.9}_{-9.4}$	743^{+151}_{-45}	[1500]	40^{+26}_{-15}
H1+H2+H4	H2	$-20.1^{+4.2}_{-10.7}$	$6.0^{+1.5}_{-2.4}$	$0.34^{+0.51}_{-0.32}$	175^{+99}_{-71}	508^{+95}_{-131}	[1500]	49^{+30}_{-23}
rms=0''15, $\chi^2 = 8.3$, k=26	H3	[-28.31]	[2.34]	[0.18]	[19.08]	88^{+46}_{-43}	43^{+53}_{-39}	$0.35^{+0.14}_{-0.34}$
$\ln(\mathcal{L}) = 14.09$, BIC=67.7	H4	$18.6^{+10.6}_{-3.8}$	$-8.1^{+2.7}_{-11.5}$	$0.19^{+0.10}_{-0.19}$	31^{+144}_{-26}	257^{+133}_{-138}	620^{+370}_{-480}	18^{+80}_{-7}
	H5	[6.69]	[-0.03]	[0]	[0]	179^{+67}_{-123}	41^{+7}_{-39}	$0.01^{+0.09}_{-0.00}$
	L*	[217]	[39]	[0.15]

Table 2. Best-fit parameters of lens models of SPT-CLJ 0356–5337. Fixed parameters are in brackets. Δ R.A. and Δ Decl. are measured relative to the reference coordinate (R.A. = 59.0895910, Decl. = -53.6311098). Ellipticity e is measured as $(a^2 - b^2)/(a^2 + b^2)$ where a and b are the semimajor and semiminor axes of the ellipse. σ_0 , r_c , and r_{cut} are the normalization, core radius, and cut radius of the halo, respectively. Uncertainties represent 95%-ile from the full MCMC sampling. All the models have the same number of constraints, $n=2 \times (\#\text{arcs} - \#\text{sources})=40$. k is the number of free parameters. χ^2 and $\ln(\mathcal{L})$ are calculated by `Lenstool` with a uniform positional uncertainty of 0''.3. Cluster scale halos H1, H2, and H4 are near the BCG, LRGs group, and the eastern outskirts, respectively; H3 is a galaxy in the LRGs group near system 4; H5 is the jellyfish galaxy. L* gives the pivot parameters of the cluster member scaling relations. See Section 4.3 and Figure 7.

of the lensing evidence, the high penalty of the BIC criterion makes the simpler models statistically favored. As we demonstrate in the following sections, some results remain consistent among models, indicating that they are robust against systematic uncertainties related to modeling choices. In particular, these include the masses of the two major sub-cluster components and their mass ratio, an important measurement for classifying the system as a major merger. Purely based on the BIC, the simplicity of model A is favoured as this model shows the lowest BIC of 32.9. We will discuss this in Section 6.

In terms of achieving a low rms, models D and E, with fixed galaxy scaling relations, perform as well as their

equivalent models with free galaxy scaling relations parameters (B and C, respectively). Formally, these models would be statistically favored over their non-fixed counterparts, as they have two fewer parameters and thus lower BIC. However, since one of the questions we are aiming to answer with the lensing analysis is the fraction of mass contained in galaxies, keeping this component fixed significantly limits our ability to investigate this question. Of these two models, the BIC criterion favors model D over E.

Assessing both criteria, we select model B as the one that best balances an adequate sampling of the parameter space, good reproduction of the lensing constraints, and lower number of free parameters. We discuss this se-

lection in Section 6. In the following sections we quote the results from model B as the best-fit model. We present the outputs of all five lens models in tables, and draw conclusions from comparing and contrasting these models. To prevent visual clutter, we only include models A, B, C, and D in the figures unless otherwise specified.

5.1. Mass distribution

Figure 9 shows the mass contours derived from the best-fit lens models A, B, C, and D. The projected mass density profile, centered on the BCG, is shown in Figure 11.

The total projected mass of the cluster, measured within 500 kpc of the BCG, is $M(<500 \text{ kpc}) = 3.75_{-0.34}^{+0.4} \times 10^{14} M_{\odot}$ (cylindrical mass), derived from model B (see Table 3 for results from all models). We note that the 95th-percentile statistical uncertainties underestimate the true uncertainty at this radius, as the measurement out to 500 kpc extends beyond the strong lensing regime. Regardless, the discovery of new multiple images outside the region between the main two halos provides constraining power on the location and extent of these halos, leading to a more accurate and precise mass estimate than was previously possible. Overall the statistical uncertainties are reduced by at least 50% compared to previous work.

We measured the masses of the different sub-cluster components (the “BCG cluster core”, hereafter BCG, and the “LRGs core”, hereafter LRGs) by summing the projected mass density output of the strong lensing models inside an aperture with a radius of 80 kpc, centered on each component. The BCG component is centered on the BCG at R.A. = 59.0895910, Decl. = -53.6311098 , and the LRGs component is centered on the brightest cluster member galaxy in the group, at R.A. = 59.079727, Decl. = -53.630291 . Following Mahler et al. (2020), we used a projected radius of 80 kpc because it encloses each component without overlapping with the other. We calculated uncertainties using a 95% confidence interval.

We find that the mass of the BCG cluster core is $M_{BCG}(<80 \text{ kpc}) = 3.93_{-0.14}^{+0.21} \times 10^{13} M_{\odot}$, the mass of the LRGs core is $M_{LRG}(<80 \text{ kpc}) = 2.92_{-0.23}^{+0.16} \times 10^{13} M_{\odot}$, and their mass ratio is $1 : 1.35_{-0.06}^{+0.16}$, all from model B. We find similar results for the masses and mass ratios for all the models considered in this work; they are listed in Table 3 and presented in Figure 8. The statistical uncertainties are estimated from the MCMC sampling of the parameter space. To account for possible correlations between the masses within the model, in calculations of mass ratios we first calculated the mass ratio in

each sampled step in the MCMC, and then determine the 95% uncertainty. The implications of this result are discussed in Section 6.

The parametric nature of the lens model algorithm allows us to consider an alternative approach, by disentangling the contributions from different components and calculating their masses analytically. To estimate the mass ratio of the two main cores, we calculated the mass within 160 kpc of H1 and the BCG, and compared it with H2 and the 8 brightest LRGs in the LRG group, using their dPIE parameterization and equations A10 and A25 in Elíasdóttir et al. (2007). The projected radius of 160 kpc was chosen as it the largest aperture that is well-constrained by strong lensing. We then compared the mass of H1 plus the BCG to that of H2 plus the 8 LRGs, to obtain the mass ratios of the two main cores, resulting with 3.2 ± 1.2 . The 95% uncertainty was derived from repeating the calculation with parameters from each sample step in the MCMC. We take the “deconstructed” mass estimates and ratios with caution. As we thoroughly discuss in Section 6.3, while the total projected mass is indeed well constrained and robust against modeling choices, model degeneracies mean that the mass of any single lens component is not. The mass ratio that results from this approach is less strongly supportive of the major merger interpretation discussed below. Further exploration of the dynamical profile of the cluster for a more comprehensive 3D projection would help refine the measurement. In the following sections, we consider the measurement based on the total projected mass density enclosed in 80 kpc, for consistency with previous work.

6. DISCUSSION

6.1. Evidence for a major merger scenario

Our lensing analysis indicates that there are two major mass components in this cluster, which align with the distribution of cluster member galaxies. The two components have different galaxy content – one is dominated by the BCG and the other is made up of a group of a few smaller LRGs. This result agrees with the findings of Mahler et al. (2020).

Also in agreement with Mahler et al. (2020), we find that most of the relative motion between the two components is on the plane of the sky, based on new MUSE data that yielded spectroscopic redshifts of 32 cluster members. We found 21 cluster-member galaxies within the MUSE footprint that are at $1.03 < z < 1.04$, including the BCG and nearby galaxies, and seven of the galaxies in the LRGs group. The median offset between the BCG and the LRGs group is 135 km s^{-1} . The MUSE

Model	Total	BCG sub-cluster	LRGs sub-cluster	Sub cluster ratio	Galaxy fraction
	$M(<500 \text{ kpc})$	$M_{BCG} (< 80 \text{ kpc})$	$M_{LRGs} (< 80 \text{ kpc})$		
	$[10^{14} M_{\odot}]$	$[10^{13} M_{\odot}]$	$[10^{13} M_{\odot}]$	M_{BCG}/M_{LRG}	
A	$3.57^{+0.21}_{-0.25}$	$3.88^{+0.11}_{-0.11}$	$2.74^{+0.10}_{-0.08}$	$1.42^{+0.07}_{-0.07}$	$0.18^{+0.06}_{-0.05}$
B	$3.75^{+0.40}_{-0.34}$	$3.93^{+0.21}_{-0.14}$	$2.92^{+0.16}_{-0.23}$	$1.35^{+0.16}_{-0.08}$	$0.15^{+0.08}_{-0.03}$
C	$3.66^{+0.36}_{-0.36}$	$3.90^{+0.14}_{-0.14}$	$3.05^{+0.13}_{-0.27}$	$1.28^{+0.14}_{-0.04}$	$0.18^{+0.02}_{-0.08}$
D	$3.72^{+0.39}_{-0.26}$	$3.98^{+0.21}_{-0.06}$	$2.97^{+0.11}_{-0.21}$	$1.34^{+0.14}_{-0.03}$	0.1 ± 0.01
E	$3.72^{+0.45}_{-0.18}$	$4.09^{+0.13}_{-0.21}$	$2.89^{+0.18}_{-0.17}$	$1.41^{+0.07}_{-0.10}$	0.1 ± 0.01

Table 3. Total projected mass density (cylindrical mass) of the cluster as a whole, and the sub-clusters and their ratio, measured from the outputs of different lens models. Despite the different modeling choices, these measurements are in excellent agreement between models. Statistical uncertainties are 95% confidence interval. The sub-cluster masses are measured within 80 kpc from the BCG and the brightest galaxy in the LRGs group. The total cluster mass and galaxy fraction are measured within 500 kpc. Note that the galaxies component in Model D and E assumed a fixed scaling relation, resulting in a mass fraction of $\sim 10\%$ that was not constrained by the lens model. See Figure 8 for a visualization, and Section 6 for a discussion of these results.

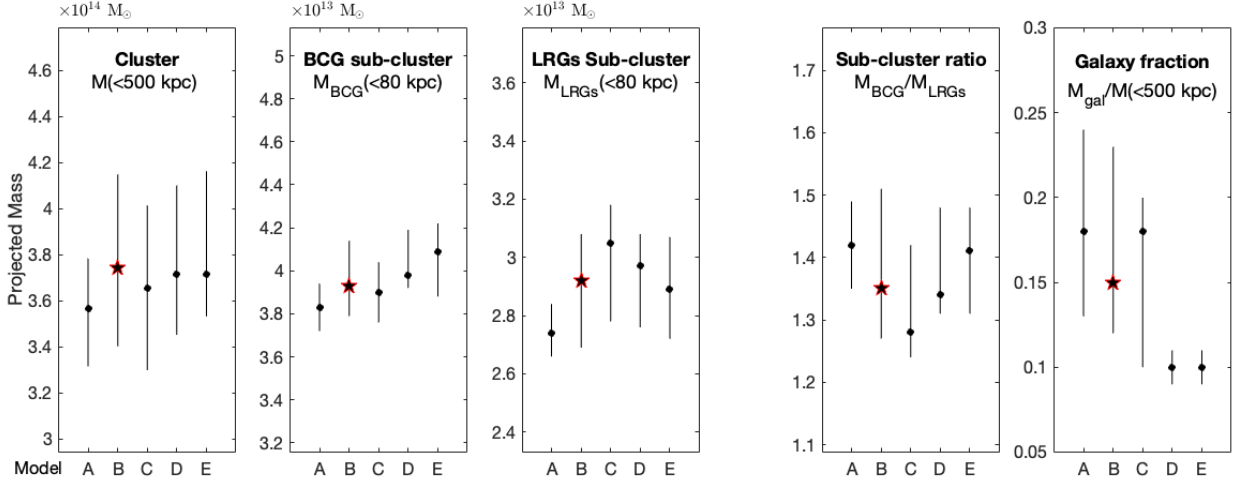


Figure 8. Mass and mass fraction from the different lens models presented in this work. From left to right: The total mass of the cluster measured as projected (cylindrical) mass within 500 kpc from the BCG; the mass measured within 80 kpc from the BCG; the mass measured within 80 kpc from the brightest galaxy in the LRG core; the ratio of the two sub-clusters; and the mass fraction contained within galaxy-scale halos. The galaxy mass fraction includes the individually-optimized galaxies (H3 near system 4, and the jellyfish galaxy H5). The datapoints match the values listed in Table 3 and their 95% confidence interval. The red star symbols highlight our fiducial model (model B). Measured masses and sub-cluster mass ratio agrees amongst all models within the uncertainties. The galaxy fraction differs between models mainly due to modelling choices, model D and E have a fixed galaxy scaling relation and only allow the cluster scale potential to vary. Model B results with a galaxy fraction slightly lower than the other models.

spectroscopy that is presented in this paper will be used in a future dynamical investigation of this cluster.

Dawson et al. (2012) presented four criteria for observing two sub-clusters during a dissociative major merger event: 1) The two components have comparable mass; 2) The two components have a small impact parameter; 3) The cluster is observed during the period where cluster gas is significantly offset from the galaxies and DM; 4) The motion of the components is mostly transverse, so that the apparent angular separation of the gas from the galaxies and DM is maximized. In this paper, we demonstrate that SPT-0356 satisfies criteria 1), 2), and

4): The mass ratio between the two major components of the cluster of 1 : 1.35 (Section 5) implies that the two components have comparable mass, thus satisfying the first criterion. This conclusion is robust to modeling assumptions. The separation on the plane of the sky is small, $\sim 21''$, or ~ 170 kpc, satisfying the second criterion. The similar redshift of the components satisfies the fourth. Further data are required to study the gas component and determine the dynamical state of the merger. This can be done with X-ray data: two distinct X-ray components associated with the two DM components would indicate that the cluster is in a pre-

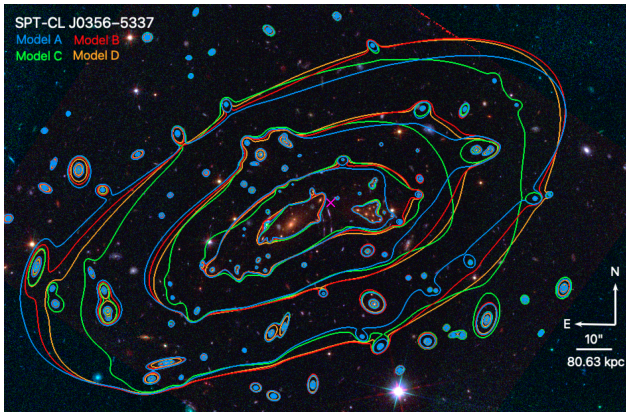


Figure 9. Mass contours overlaid on the HST imaging for models A, B, C, and D in blue, red, green, and orange, respectively. The contours are plotted at projected mass densities of 0.25 , 0.5 , 1 and $2 \times 10^9 M_{\odot} \text{kpc}^{-2}$. The magenta cross marks the centroid the X-ray emission (Mahler et al. in prep.)

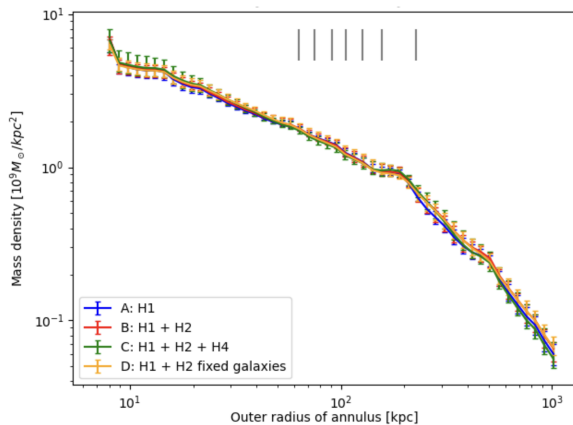


Figure 10. Total projected mass density profiles for the range of models investigated in this paper. The average mass densities are measured in annuli centered on the BCG. The “bump” at ~ 200 kpc corresponds to the LRGs structure. Uncertainties are 95% confidence interval, derived from the MCMC sampling of the parameter space. The projected distances of the lensing constraints are indicated with gray ticks.

merger phase; a single X-ray peak between the mass components would indicate a recent merger (e.g., Clowe et al. 2006). An analysis of the Chandra X-ray data obtained by program ID #22800530 (PI: Mahler) will be presented in a future work. Preliminary results indicate that the centroid of the X-ray emission is consistent with being between the two halos (Figure 9).

6.2. Comparison to Previous Work

Mahler et al. (2020) published the first strong lensing analysis and lens model of SPT-0356, as described above, using ground-based imaging data and multislit

spectroscopy, and a single-band HST image. With the data available at the time, they were able to identify three sets of arcs to be used as lensing constraints, all of which appear between the two sub-clusters. The main improvements offered by the current work are the increased quantity and distribution of lensing constraints, and spectroscopic redshifts of numerous objects in the cluster core, enabled by the multiband HST imaging and VLT/MUSE IFU spectroscopy. The new data also facilitated a better selection of cluster-member galaxies to be included in the lens model, increasing their number from 45 to 149. We note that the higher rms in the new model is expected, because it has more arcs (Johnson & Sharon 2016).

To compare the masses of the two main sub-clusters between models, we used the model of Mahler et al. (2020) to compute the total enclosed mass within 80 kpc of the BCG and of the LRGs group, in the same way that was done in Section 5.1, and estimated the 95% confidence interval statistical uncertainties from the MCMC sampling. Obtaining these measurements directly from the lens model was necessary, since the reported numbers in Mahler et al. (2020) did not aggregate all the mass components including the different cluster-scale halos and galaxy contribution in the BCG and group, and were reported with 68% uncertainty. The Mahler et al. (2020) fiducial model (model B in their Table 4, which has one cluster halo, DM1 free, optimized BCG) yields $M_{BCG}(< 80\text{kpc}) = 4.04^{+0.07}_{-0.10} \times 10^{13} M_{\odot}$, in agreement with the new model, $M_{BCG}(< 80\text{kpc}) = 3.93^{+0.21}_{-0.14} \times 10^{13} M_{\odot}$. For the LRGs sub-cluster, the Mahler et al. (2020) fiducial model yields a higher mass than the new model, $M_{LRG}(< 80\text{kpc}) = 3.41 \pm 0.09 \times 10^{13} M_{\odot}$ compared to $M_{LRG}(< 80\text{kpc}) = 2.92^{+0.16}_{-0.23} \times 10^{13} M_{\odot}$ from our model B. The new model is in excellent agreement with models that allow more flexibility, e.g., model D in Mahler et al. (2020) that allows for a second DM halo near the LRGs, and yields $M_{LRG}(< 80\text{kpc}) = 3.01^{+0.42}_{-0.25} \times 10^{13} M_{\odot}$.

The mass within 500 kpc is in agreement with Mahler et al. (2020) within errorbars, although the new models predict a somewhat higher large-scale mass than the fiducial model of Mahler et al. (2020), likely driven by the new evidence that the strong lensing regime extends at least to the radius of arc 7 in the east. We reduced the statistical uncertainty on the total mass of the cluster (within 500 kpc) from $\sim 16\%$ in the fiducial model of Mahler et al. (2020) to $\sim 10\%$. Owing to the new constraints in the east and west, the new model improved the statistical uncertainty on the positions of individual mass components. Most notably, the previous model, which had no constraints west of the group of LRGs,

Deconstructed Mass Density Profiles of SPT-CL J0356-5337

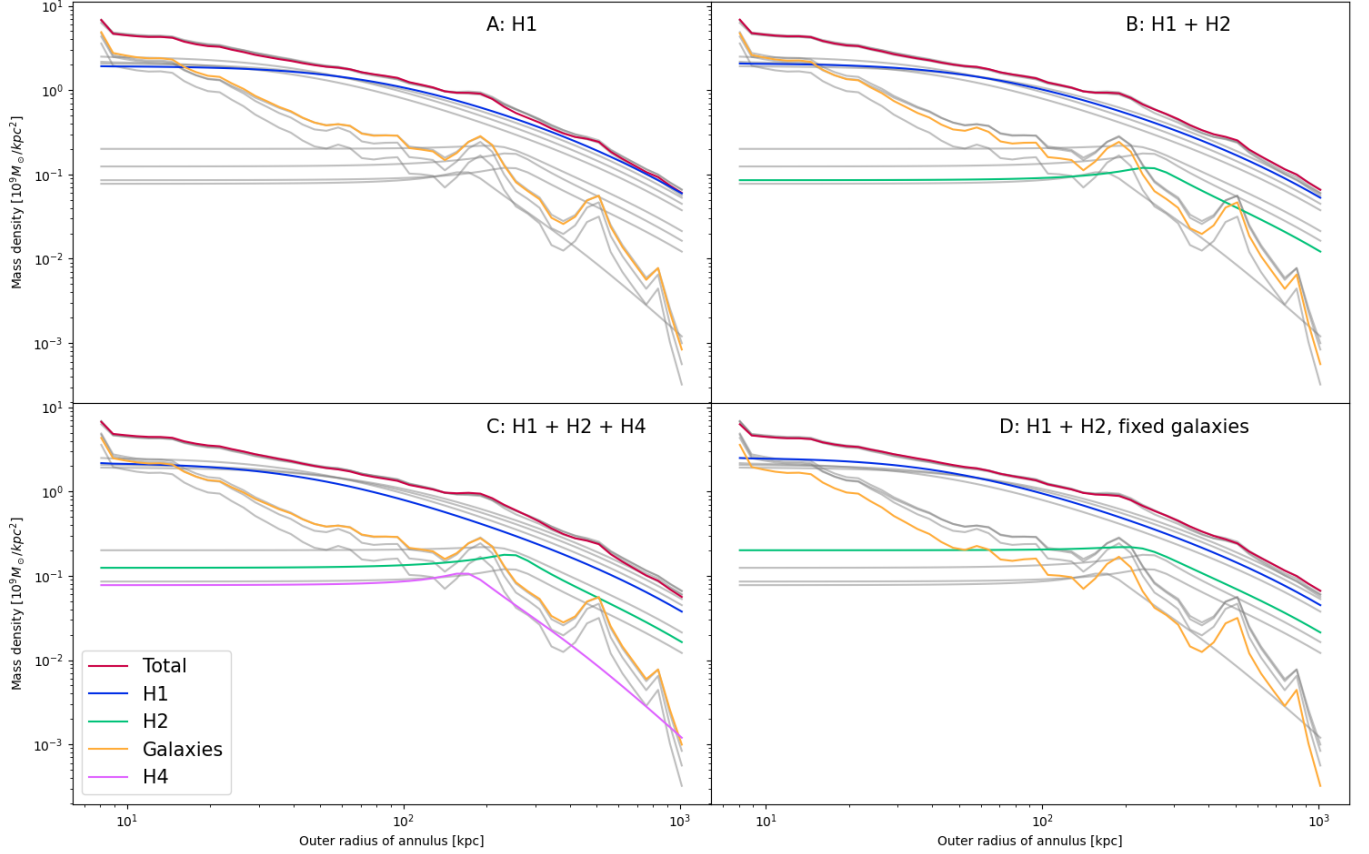


Figure 11. The projected mass density profile of the individual contributions of the major cluster halos and the galaxy component. The average mass densities are measured in annuli centered on the BCG. Uncertainties are on the order of $\sim 10\%$, but are omitted for clarity. Each panel displays the results from one of the models. The model components are color-coded as indicated in the legend. Gray lines are the same in all panels, and are plotted to facilitate a convenient comparison between the models.

suffered from a high uncertainty in the position of H2, in particular, the R.A. could only be localized to within a 25 arcsecond range. We localized the R.A. of H2 to within ~ 15 arcseconds. Additionally, all the models investigated in this paper that allow for a second cluster halo generally agree on the location of H2 within statistical uncertainties, indicating that the additional constraining power of the new system 4 (the west-most arc, See Figure 2) is driving this improvement, rather than modeling choices.

The main conclusion, that the system is composed of two sub-clusters of comparable mass, with a ratio of $\sim 1 : 1.35$, is in good agreement between the new analysis and previous work.

6.3. Mass composition and model degeneracies

The primary output of gravitational lens modeling is the distribution of projected mass density in the lens plane. One of the strengths of parametric lens modeling algorithms such as `Lenstool`, which assume that

the mass distribution is composed of the sum of several functional halos, is their ability to examine the relative contributions from different cluster components: the different major cluster halos, and the galaxy-scale halos. Figure 11 shows the contributions of the different mass components to the overall cluster mass, and aids in comparing the different mass models to each other and point out model degeneracies.

Unsurprisingly, the peak in the galaxy component profile seen at ~ 200 kpc coincides with the group of LRGs, also visible in the total mass profiles as a bump at the same radius. As can be seen in the top line in Figure 11 and the profiles plotted in Figure 10, the total projected mass profiles from the four models are nearly indistinguishable, indicating that modeling choices have little to no effect on the overall cluster radial profile.

As lensing is sensitive to the total mass regardless of its origin, lens models can distribute the mass between, e.g., the BCG and the main DM halos, or add or remove mass from cluster member galaxies by compensat-

ing elsewhere in the model. Figure 11 (deconstructed mass profiles) clearly shows this effect: a model with a lower galaxy component (D) compensates with a higher H2 mass. A model without H2 or H4 compensates by increasing the mass of H1. This explains the observation that regardless of modeling choices (one, two, or three cluster halos, fixed or free galaxy scaling relations), the total projected mass density of the sub-clusters (Table 3, Figure 8) is consistent between models.

Similarly, the relative contribution from cluster member galaxies to the total mass of the cluster (measured within 500 kpc) is consistent between models that explored the parameter space of this property, predicting a mass fraction that ranges from $0.15^{+0.01}_{-0.02}$ (model B) to $0.18^{+0.02}_{-0.02}$ (model C). However, owing to degeneracies between model parameters, the lensing analysis cannot rule out a lower mass fraction – models with a fixed galaxy contribution of 10% (models D/E) performed similarly well as models with free scaling relations parameters, indicating that this property is not well constrained by strong lensing alone in this cluster.

Examining the differences between the models in Figure 7 (visualization of mass halos), Figure 9 (mass contours), and Table 2 (model parameters) reveals more interesting insights about the effects of modeling choices and model flexibility on the overall mass distribution, and the limitations of complex mass models in determining the relative contribution of mass components. Including H4 in the lens model adds mass in the eastern region of the cluster core (Figure 7), which is required to satisfy the constraints of system 7. Models without H4 (Models A, B, D), add the needed mass in this region by slightly increasing the ellipticity and normalization of the major cluster component, H1 (e.g., compare the e and σ_0 parameters of H1 of the different models in Table 2). The effect of this compensation for the lowered flexibility in the east part of the core is seen in Figure 9 as a deviation of the contours of model C from the other models, but only outside of the region where strong lensing constraints exist, thus not significantly affecting or driving the performance of the models. The shape of the cluster mass distribution on a large scale cannot be constrained by strong lensing alone. Weak lensing can possibly help break the degeneracy between models B and C, and help constrain the large-scale ellipticity of the mass distribution, since the effects of weak lensing are observed farther out from the cluster core.

The model degeneracies also come into light when comparing the new models to the models from Mahler et al. (2020). That work evaluated models with H1 and a free BCG halo, with and without H2. Table 4 in that paper shows, for example, that the two models with sim-

ilar rms have vastly different ratios of H1, H2, and BCG contributions – the model with H1 fixed to the location of the BCG resulted with a very low BCG normalization, attributing its mass to the coincident cluster DM halo. As noted in Section 4.3, the conclusion of our attempts to free the BCG parameters was that the added flexibility is not justified, as models with free BCG parameters do not perform better than models with the BCG using the same scaling relations as the other red-sequence galaxies.

These degeneracies indicate that we are unable to tightly constrain the relative contributions of mass components, or the percentage of cluster mass contained in galaxies. We are also unable to constrain the shape of the model outside of where we have strong lensing constraints, as the same results can be produced by adding mass or increasing ellipticity. Additional constraints provided by weak lensing could aid in this endeavor and offer more insight into the geometry of this cluster.

6.4. Physical and statistical criteria of model selection

We present in this analysis 5 lens models with different levels of complexity. To assess these models we used two criteria (Section 5): the rms, which is directly linked to the goodness of fit, and the BIC, which is broadly used in Bayesian analyses to select between a finite set of models where over-fitting is a concern (for previous work that used BIC in strong lens modeling analysis, see, e.g., Mahler et al. 2018, 2020; Acebron et al. 2022; Biviano et al. 2023). In this section, we discuss the use of the BIC criterion and contrast it with physical considerations for discriminating between models, while keeping in mind that our lens modeling aims to reproduce the mass distribution of a cluster of galaxies. All models used the exact same number of constraints, i.e., $\ln(n) = \ln(40)$ is a constant in all models. Therefore, the BIC effectively quantifies the extent to which additional free parameters are able to maximize the $\ln(L)$ (for a definition of the likelihood function in `Lenstool`, we refer the reader to Jullo et al. 2007; Niemiec et al. 2020). It is to be noted that a difference in BIC of > 10 is considered strong (Kass & Raftery 1995; Lorah & Womack 2019) and a difference in BIC of < 2 is not significant.

Model B produced a lower rms than model A (rms = $0''.17$ vs. rms = $0''.20$) therefore it provides a better fit to the data that, while a small differences, could be argued to be significant. The lower BIC favors model A, which is the most simplistic of the five models under assessment, with one halo located near the BCG. Using the BIC straightforwardly (or naively) for selecting our model would mean that adding one more free clus-

ter scale potential (6 free parameters) at the location of the LRGs is considered to be over-fitting, increasing the BIC from 32.9 (model A) to 50.9 (model B). However, we can provide a physical argument that model A has the largest offset between the center of the cluster scale potential and the BCG as well as the largest position angle misalignment compare to every other model reported in this analysis. We can reason that the model is trying to compensate for the mass lacking in the LRG location with H1, to achieve the fixed total mass needed to satisfy the lensing constraints. As we demonstrated in Table 3, the projected mass within 80 kpc is consistent between models regardless of whether H2 is included. While it is expected that cluster halos and BCGs tend to align with each other (Lambas et al. 1988; Ragone-Figueroa et al. 2020) and we are still well within the range of possible even in model A, we stress that in every other model tested here, when given the flexibility to do so, H1 tends to better align with BCG morphology.

Comparing model B and model D offers insights into the ability of the BIC to consider the effect of allowing the scaling relation of cluster member galaxies to vary. The difference of about 7 in BIC estimate tend to slightly favour model D with a fixed scaling relation over model B, since it has a similar goodness of fit and 2 fewer parameters. We argue here that allowing the scaling relation to vary is essential for examining the degeneracy among the sub-component of a models. Model B is better able to capture the underlying uncertainties in the distribution of dark matter within the clusters itself. We again stress that the strong lensing configuration is giving a robust estimate of the total amount of mass within 80 kpc regardless of the model. However, the model with the galaxy-scaling relation free to vary is probing a more diverse parameter space. Fixing these parameters could lead to an incomplete account of the statistical error budget.

Model C presents the best fit to the data with the lowest rms of $0''.14$; it is however disfavored by having the highest BIC. Naively, this model could be discarded on the basis of its high BIC (73.7), suggesting that it over-fits the data by including halo H4. However, an inspection of the projected mass density contours of the cluster as presented in Figure 9 reveals that the change in shape is most prominent at the outskirts. As previously mentioned, the contours in the outskirts of all other models (A, B, and D, which do not include H4) are showing very elliptical mass distribution, matching the ones from H1 at the very edge, beyond the strong lensing region. Model C has a more complex mass distribution with a significantly lower ellipticity on large scales. As previously mentioned we cannot with strong

lensing data alone constrain the morphology of this cluster far beyond the strong lensing regime but we again stress that the sole use of BIC is preventing exploration of the model and should be considered alongside physical consideration when selecting favoured models.

7. SUMMARY

We present new multi-band HST imaging and a strong lensing analysis of SPT-CLJ 0356–5337, a galaxy cluster at redshift $z = 1.034$. We build upon and improve the initial lens model constructed by Mahler et al. (2020) by identifying additional lensing constraints, including two new lensed galaxies with spectroscopic redshifts, for a total of five high-confidence lensed sources with multiple images, and several candidate arcs. We used the resulting lens models to estimate the mass ratio of the two main components of SPT-0356, with the goal of confirming its classification as a major merger.

We also report in this paper the serendipitous discovery of a background group of three doubled-peaked Ly α emitting galaxies at $z = 4.1448$, magnified by a factor of 2–4 by the cluster. Ly α emission is also detected in three of the strongly-lensed galaxies, at $z = 3.048$, $z = 3.0205$, and $z = 5.3288$.

The multi-band HST imaging and MUSE spectroscopy resulted in the robust identification of constraints in previously underconstrained areas of the lens, most importantly, east of the BCG and west of the LRGs, which allows us to better constrain the projected mass density distribution of the cluster. The galaxy distribution and the lensing geometry indicate that the cluster has at least two major cores. We found that a mass model with two cluster-scale halos adequately reproduces the lensing evidence, while keeping the number of free parameters low. We explored a possibility that the lens plane is more complex, by allowing a flexible third halo (H4). A model with three cluster-scale halos does produce a lower image plane rms, however, a BIC analysis determined that the slight improvement in rms is not justified by the number of added parameters. We therefore selected model B as a sufficient representation of the lens plane given the available constraints. Further constraints on the large scale ellipticity of the cluster from weak lensing can help break the degeneracy between models.

We used the derived lens models to calculate the total projected mass density enclosed within a radius of 80 kpc centered on each of the sub-clusters, the “BCG” core and the “LRGs” core. The sub-cluster masses are $M_{BCG}(< 80\text{kpc}) = 3.93_{-0.14}^{+0.21} \times 10^{13} M_{\odot}$ and $M_{LRG}(< 80\text{kpc}) = 2.92_{-0.23}^{+0.16} \times 10^{13} M_{\odot}$ for the BCG core and LRGs core, respectively. The total mass of the cluster,

measured as projected (cylindrical) mass within 500 kpc from the BCG, is $M(<500 \text{ kpc})=3.75_{-0.34}^{+0.4} \times 10^{14} M_{\odot}$. We find that despite making different assumptions on the number of subhalos, all models have consistent mass ratio results, yielding a mass ratio between 1:1.28 and 1:1.42, and support the classification of SPT-0356 as a major merger, in agreement with Mahler et al. (2020). Combined with the small separation of the sky (~ 170 kpc) and the small radial velocity offset (135 km s^{-1}), we conclude that the cluster is observed during a major merger on the plain of the sky.

Future analysis using X-ray data and advanced dynamical study of the cluster core could classify this cluster as a dissociative merger, which would make it a unique target to probe large-scale structure formation, cluster assembly and galaxy evolution in the densest nodes of the cosmic web.

This research is based on observations made with the NASA/ESA Hubble Space Telescope obtained from the Space Telescope Science Institute, which is operated by the Association of Universities for Research in Astronomy, Inc., under NASA contract NAS 5-26555. These observations are associated with programs GO-16425, GO-13412. Support for program # 16425 was provided by NASA through a grant from the Space Telescope Science Institute, which is operated by the Association of Universities for Research in Astronomy, Inc., under NASA contract NAS 5-03127. Based on observations collected at the European Southern Observatory under ESO programme 106.21JF.001 obtained from the ESO Science Archive Facility. The South Pole Telescope program is supported by the National Science Foundation (NSF) through awards OPP-1852617 and 2332483. Partial support is also provided by the Kavli Institute of Cosmological Physics at the University of Chicago. Work at Argonne National Lab is supported by UChicago Argonne LLC, Operator of Argonne National Laboratory (Argonne). Argonne, a U.S. Department of Energy Office of Science Laboratory, is operated under contract no. DE-AC02-06CH11357.

Facilities: HST(ACS, WFC3), VLT(MUSE)

Software: Source Extractor (Bertin & Arnouts 1996); Lenstool (Jullo et al. 2007); AstroDrizzle (Fruchter & et al. 2010); Matlab (Inc. 2022); Astropy (Astropy Collaboration et al. 2018); MATLAB Astronomy and Astrophysics Toolbox (MAAT; Ofek 2014)

REFERENCES

- Acebron, A., Grillo, C., Bergamini, P., et al. 2022, A&A, 668, A142, doi: [10.1051/0004-6361/202244836](https://doi.org/10.1051/0004-6361/202244836)
- Astropy Collaboration, Price-Whelan, A. M., Sipőcz, B. M., et al. 2018, AJ, 156, 123, doi: [10.3847/1538-3881/aabc4f](https://doi.org/10.3847/1538-3881/aabc4f)
- Bacon, R., Piqueras, L., Conseil, S., Richard, J., & Shepherd, M. 2016, MPDAF: MUSE Python Data Analysis Framework, Astrophysics Source Code Library, record ascl:1611.003
- Bacon, R., Accardo, M., Adjali, L., et al. 2010, in Society of Photo-Optical Instrumentation Engineers (SPIE) Conference Series, Vol. 7735, Ground-based and Airborne Instrumentation for Astronomy III, ed. I. S. McLean, S. K. Ramsay, & H. Takami, 773508, doi: [10.1117/12.856027](https://doi.org/10.1117/12.856027)
- Bacon, R., Conseil, S., Mary, D., et al. 2017, A&A, 608, A1, doi: [10.1051/0004-6361/201730833](https://doi.org/10.1051/0004-6361/201730833)
- Bertin, E., & Arnouts, S. 1996, A&AS, 117, 393, doi: [10.1051/aas:1996164](https://doi.org/10.1051/aas:1996164)
- Biviano, A., Pizzuti, L., Mercurio, A., et al. 2023, ApJ, 958, 148, doi: [10.3847/1538-4357/acf832](https://doi.org/10.3847/1538-4357/acf832)
- Bleem, L. E., Stalder, B., de Haan, T., et al. 2015, ApJS, 216, 27, doi: [10.1088/0067-0049/216/2/27](https://doi.org/10.1088/0067-0049/216/2/27)
- Bleem, L. E., Bocquet, S., Stalder, B., et al. 2020, ApJS, 247, 25, doi: [10.3847/1538-4365/ab6993](https://doi.org/10.3847/1538-4365/ab6993)
- Bocquet, S., Dietrich, J. P., Schrabback, T., et al. 2019, ApJ, 878, 55, doi: [10.3847/1538-4357/ab1f10](https://doi.org/10.3847/1538-4357/ab1f10)
- Bradač, M., Allen, S. W., Treu, T., et al. 2008, ApJ, 687, 959, doi: [10.1086/591246](https://doi.org/10.1086/591246)
- Bradač, M., Clowe, D., Gonzalez, A. H., et al. 2006, ApJ, 652, 937, doi: [10.1086/508601](https://doi.org/10.1086/508601)
- Caminha, G. B., Grillo, C., Rosati, P., et al. 2023, A&A, 678, A3, doi: [10.1051/0004-6361/202244897](https://doi.org/10.1051/0004-6361/202244897)

- Clowe, D., Bradač, M., Gonzalez, A. H., et al. 2006, *ApJL*, 648, L109, doi: [10.1086/508162](https://doi.org/10.1086/508162)
- Dawson, W. A., Wittman, D., Jee, M. J., et al. 2012, *ApJL*, 747, L42, doi: [10.1088/2041-8205/747/2/L42](https://doi.org/10.1088/2041-8205/747/2/L42)
- Elíasdóttir, Á., Limousin, M., Richard, J., et al. 2007, arXiv e-prints, arXiv:0710.5636, doi: [10.48550/arXiv.0710.5636](https://doi.org/10.48550/arXiv.0710.5636)
- Fakhouri, O., & Ma, C.-P. 2008, *MNRAS*, 386, 577, doi: [10.1111/j.1365-2966.2008.13075.x](https://doi.org/10.1111/j.1365-2966.2008.13075.x)
- Fruchter, A. S., & et al. 2010, in 2010 Space Telescope Science Institute Calibration Workshop, 382–387
- Fumagalli, M., Cantalupo, S., Dekel, A., et al. 2016, *MNRAS*, 462, 1978, doi: [10.1093/mnras/stw1782](https://doi.org/10.1093/mnras/stw1782)
- Fumagalli, M., Mackenzie, R., Trayford, J., et al. 2017, *MNRAS*, 471, 3686, doi: [10.1093/mnras/stx1896](https://doi.org/10.1093/mnras/stx1896)
- Gladders, M. D., & Yee, H. K. C. 2000, *AJ*, 120, 2148, doi: [10.1086/301557](https://doi.org/10.1086/301557)
- Harvey, D., Massey, R., Kitching, T., Taylor, A., & Tittley, E. 2015, *Science*, 347, 1462, doi: [10.1126/science.1261381](https://doi.org/10.1126/science.1261381)
- Inc., T. M. 2022, MATLAB version: 9.13.0 (R2022b), Natick, Massachusetts, United States: The MathWorks Inc. <https://www.mathworks.com>
- Johnson, T. L., & Sharon, K. 2016, *ApJ*, 832, 82, doi: [10.3847/0004-637X/832/1/82](https://doi.org/10.3847/0004-637X/832/1/82)
- Jullo, E., Kneib, J. P., Limousin, M., et al. 2007, *New Journal of Physics*, 9, 447, doi: [10.1088/1367-2630/9/12/447](https://doi.org/10.1088/1367-2630/9/12/447)
- Kass, R. E., & Raftery, A. E. 1995, *Journal of the American Statistical Association*, 90, 773, doi: [10.1080/01621459.1995.10476572](https://doi.org/10.1080/01621459.1995.10476572)
- Lambas, D. G., Groth, E. J., & Peebles, P. J. E. 1988, *AJ*, 95, 996, doi: [10.1086/114695](https://doi.org/10.1086/114695)
- Lorah, J., & Womack, A. 2019, *Behavior Research Methods*, 51, 440, doi: [10.3758/s13428-018-1188-3](https://doi.org/10.3758/s13428-018-1188-3)
- Mahler, G., Richard, J., Clément, B., et al. 2018, *MNRAS*, 473, 663, doi: [10.1093/mnras/stx1971](https://doi.org/10.1093/mnras/stx1971)
- Mahler, G., Sharon, K., Gladders, M. D., et al. 2020, *ApJ*, 894, 150, doi: [10.3847/1538-4357/ab886b](https://doi.org/10.3847/1538-4357/ab886b)
- Markevitch, M., Gonzalez, A. H., Clowe, D., et al. 2004, *ApJ*, 606, 819, doi: [10.1086/383178](https://doi.org/10.1086/383178)
- Menanteau, F., Hughes, J. P., Sifón, C., et al. 2012, *ApJ*, 748, 7, doi: [10.1088/0004-637X/748/1/7](https://doi.org/10.1088/0004-637X/748/1/7)
- Niemiec, A., Jauzac, M., Jullo, E., et al. 2020, *MNRAS*, 493, 3331, doi: [10.1093/mnras/staa473](https://doi.org/10.1093/mnras/staa473)
- Ofek, E. O. 2014, MAAT: MATLAB Astronomy and Astrophysics Toolbox, Astrophysics Source Code Library, record ascl:1407.005. <http://ascl.net/1407.005>
- Ragone-Figueroa, C., Granato, G. L., Borgani, S., et al. 2020, *MNRAS*, 495, 2436, doi: [10.1093/mnras/staa1389](https://doi.org/10.1093/mnras/staa1389)
- Randall, S. W., Markevitch, M., Clowe, D., Gonzalez, A. H., & Bradač, M. 2008, *ApJ*, 679, 1173, doi: [10.1086/587859](https://doi.org/10.1086/587859)
- Schwarz, G. 1978, *The Annals of Statistics*, 6, 461, doi: [10.1214/aos/1176344136](https://doi.org/10.1214/aos/1176344136)
- Soto, K. T., Lilly, S. J., Bacon, R., Richard, J., & Conseil, S. 2016, *MNRAS*, 458, 3210, doi: [10.1093/mnras/stw474](https://doi.org/10.1093/mnras/stw474)
- Weilbacher, P. 2015, in *Science Operations 2015: Science Data Management*, 1, doi: [10.5281/zenodo.34658](https://doi.org/10.5281/zenodo.34658)
- Wittman, D., Golovich, N., & Dawson, W. A. 2018, *ApJ*, 869, 104, doi: [10.3847/1538-4357/aaee77](https://doi.org/10.3847/1538-4357/aaee77)